

Article

# Characterization of the Effects of Ingested Bodies on the Rotor–Stator Interaction of Hydraulic Turbines

Alfredo Guardo \*, Alfred Fontanals, Mònica Egusquiza, Carme Valero and Eduard Egusquiza

Centre de Diagnòstic Industrial i Fluidodinàmica, Universitat Politècnica de Catalunya BarcelonaTECH (UPC-CDIF), Av. Diagona 647, 08028 Barcelona, Spain; alfred.fontanals@upc.edu (A.F.); monica.egusquiza@upc.edu (M.E.); m.del.carmen.valero@upc.edu (C.V.); eduard.egusquiza@upc.edu (E.E.)

\* Correspondence: alfredo.guardo-zabaleta@upc.edu

**Abstract:** Runner and distributor blockages in hydraulic turbines occur due to the ingestion of external bodies such as rocks or logs. These obstructions can change the amplitude and uniformity of the pressure pulsations in the machine, creating large unbalanced forces that can lead to reduced efficiency, increased vibration and mechanical damage. In this paper, the effects of obstructions caused by ingested bodies in the runner and the distributor of a pump turbine on its internal pressure pulsation were investigated by means of computational fluid dynamics. A numerical model of an unobstructed pump turbine is presented and validated against experimental data. Several cases of runner or distributor blockage were studied, and their RSI pressure pulsations were recorded and analyzed at different locations. The results obtained allow us to characterize the effect of these blockages on the machine's RSI, which can be helpful for the correct diagnosis of these types of damage.

**Keywords:** turbine failure; ingested bodies; runner blockage; rotor–stator interaction; vibration; computational fluid dynamics

**Citation:** Guardo, A.; Fontanals, A.; Egusquiza, M.; Valero, C.; Egusquiza, E. Characterization of the Effects of Ingested Bodies on the Rotor–Stator Interaction of Hydraulic Turbines. *Energies* **2021**, *14*, 6669. <https://doi.org/10.3390/en14206669>

Academic Editor: Chirag Trivedi

Received: 24 August 2021

Accepted: 8 October 2021

Published: 14 October 2021

**Publisher's Note:** MDPI stays neutral with regard to jurisdictional claims in published maps and institutional affiliations.



**Copyright:** © 2021 by the authors. Licensee MDPI, Basel, Switzerland. This article is an open access article distributed under the terms and conditions of the Creative Commons Attribution (CC BY) license (<http://creativecommons.org/licenses/by/4.0/>).

## 1. Introduction

Hydropower is one of the key players in the transition to a carbon-free global energy scenario. With the ever-increasing share of electricity coming from renewable sources of variable nature, such as wind and solar, hydropower plants are increasingly required to operate in a flexible way. This means they must supply or take energy from the grid according to fluctuating demands, and to do so, their availability and reliability must be guaranteed [1].

The core element of a hydropower plant is the turbine, which converts the potential energy of the water into electrical energy. Turbines are regarded as the main asset of power plants, and the utility operators need to maximize their profitability. One of the situations to be avoided at all costs is the impairment of the machine due to abnormal operation or damage of any of its components. To avoid large economic losses, it is thus essential to rapidly detect the situations that can put the proper operation of the turbine or its structural integrity in jeopardy.

Hydropower plants take advantage of the potential energy of water contained in a high-altitude reservoir with respect to a lower one. By means of a hydraulic conduit or penstock, the water is connected between both reservoirs and used to rotate a turbine installed near the bottom. In Figure 1, the main components of a reaction hydraulic turbine are represented.

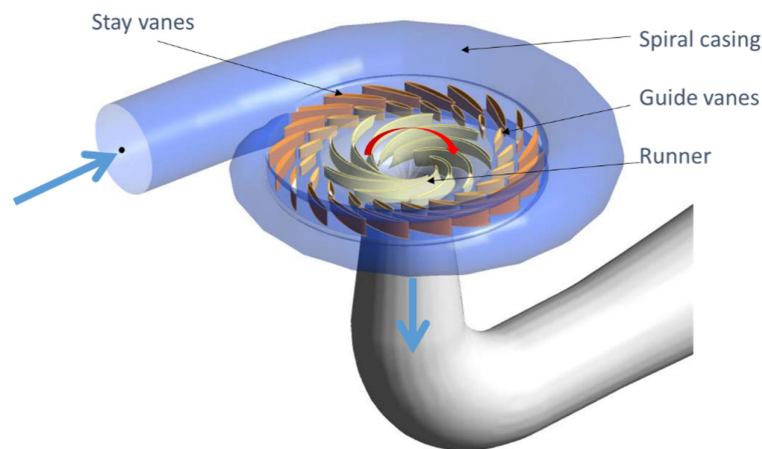


**Figure 1.** Main components of a reaction hydraulic turbine.

Damage mechanisms in hydraulic turbines have been reviewed in recent years [2]. In reaction turbines (such as Francis turbines or pump turbines), damage is typically a result of problems such as material fatigue [3–6], cavitation [7] or sediment erosion [8], which may deteriorate both the runner and distributor, taking its toll on the remaining useful life of the machine.

Material fatigue is a common form of failure mode in hydraulic turbines [3]. The turbine components, which are usually subjected to cyclic mechanical stresses below the normal yield strength, fail progressively by cracking [9]. In some cases, this deformation is caused by the dynamic/vibratory response of the runner to hydrodynamic forces and pressure pulsation during the machine operation [4]. The turbine assembly, formed by various interconnected components, can transfer mechanical vibration from one of the members to others, leading to deformation in all the components [5]. Turbine materials regularly subjected to vibration may result in material failure due to fatigue [3].

Cavitation occurs due to the formation of vapor bubbles and their subsequent burst resulting from changes in the fluid pressure in regions usually near the rotor blades or close to the exit of the turbine, where there are large differences between the static and dynamic components of the fluid pressure [2]. The repeated formation and collapse of these vapor bubbles deteriorates the surface of the machine components due to pitting action [9], and it has been reported that surface penetration due to cavitation damage can reach up to 10 mm per year on the surfaces of critical components such as impellers, turbine blades and casings [10].

Erosion is the gradual removal of material from the surface of a component as a result of repeated deformation and cutting action [11]. The erosive wear of turbine components is the result of flows of a high velocity and impingement of abrasive sediments on the surface of the turbines [12], which leads to the formation of surface irregularities in the flow guiding surfaces, initiating cavitation-type effects on the turbine unit [9]. This wear is directly proportional to the sediment size and its mineral content [9,13].

It is not uncommon, though, for the machine to be impaired due to other causes such as the ingestion of external bodies. Turbines absorb large amounts of water, which may carry small particles as well as large pieces of wood, stones or dead animals. In case these pass through at the top of the penstock due to trash rack failure [14], they will collide with the turbine, causing direct damage. It is also possible that they remain stuck between the vanes of the distributor or the blades of the runner. If so, the distribution of hydraulic forces may be modified, leading to problems after some time of operation. Failures due to ingested bodies were studied in detail by Egusquiza et al. (2010) [15]. With the analysis of several historical cases, they concluded that runner blockage increases the hydraulic unbalance, while distributor blockage leads to a significant increase in the blade passing

frequency. However, the effect of the size and position of the extraneous bodies was not determined.

In this paper, the effects of obstruction in the runner and the distributor of a pump turbine were investigated for different blockage sizes and positions. With a numerical model validated with experimental data, the pressure pulsations were analyzed for the following cases: three different blockage sizes in the runner (25, 50 and 75% of the rotor channel cross-section area), three different blockage positions in the runner channel (at 0.4, 0.6 and 0.8 the diameter of the runner) and two different sizes of obstruction between the guide vanes of the distributor (50% and 100% of the distributor channel cross-section area).

## 2. Methodology

### 2.1. Case Study

A geometrically similar scaled model of the pump turbine prototype studied in [15] was created by means of computational fluid dynamics (CFD). Details of the pump turbine prototype can be found in Section 3.1. The scaled model consisted of a runner with diameter  $D = 510$  mm and  $z_b = 7$  blades, and a distributor with  $z_v = 16$  guide and stay vanes, rotating at  $N = 3435$  rpm, maintaining the prototype's dimensionless specific speed  $N_s = 0.7048$ .

Rotor–stator interaction (RSI) characteristic frequencies for turbomachinery can be obtained from Equations (1)–(3),  $n$  being an arbitrary, positive integer used to represent the harmonics [16].

$$f_f = N/60 \quad (1)$$

$$f_b = n \cdot f_f \cdot z_b \quad (2)$$

$$f_v = n \cdot f_f \cdot z_v \quad (3)$$

The case study characteristic RSI frequencies are the runner rotation frequency  $f_f = 57.25$  Hz, the rotor blade frequency  $f_b = n \cdot 400.75$  Hz (observed in the inertial reference frame) and the distributor vane frequency  $f_v = n \cdot 916$  Hz (observed in the rotating reference frame).

### 2.2. Geometry and Mesh

Computational models for all studied cases were generated using a sliding mesh technique [17]. The computational domain studied consisted of three control volumes (distributor, runner and draft tube) linked by numerical interfaces (Figure 2).

Tetrahedral meshes were created for both the turbine model runner and distributor. Mesh independency was tested by means of steady-state simulations, determining pressure drops through rotor and distributor control volumes for best efficiency point (BEP) (0.953 m<sup>3</sup>/s flow rate, obtained through similarity analysis of the prototype's BEP) operating conditions. The tested mesh element sizes ranged from 3 to 10 mm. Mesh independency was achieved at around 4900 kEl for the rotor, and 4300 kEl for the distributor, corresponding to average element sizes of 6 mm and 5 mm, respectively. A boundary layer mesh, with  $60 < y^+ < 300$ , was attached to both distributor vanes and rotor blades, and an elbow-type draft tube with varying cross-sections with a 340 kEl hexahedral mesh was included in the computational model. The addition of a draft tube improves the runner pressure results in turbine CFD models by allowing pressure recovery downstream [18].

Obstructions caused by ingested bodies were modeled as a reduction in the free cross-section area in the distributor and runner channels (Figure 3). Runner obstructions were set to 25, 50 or 75% channel blockage, while distributor obstructions were set to 50 or 100% channel blockage.

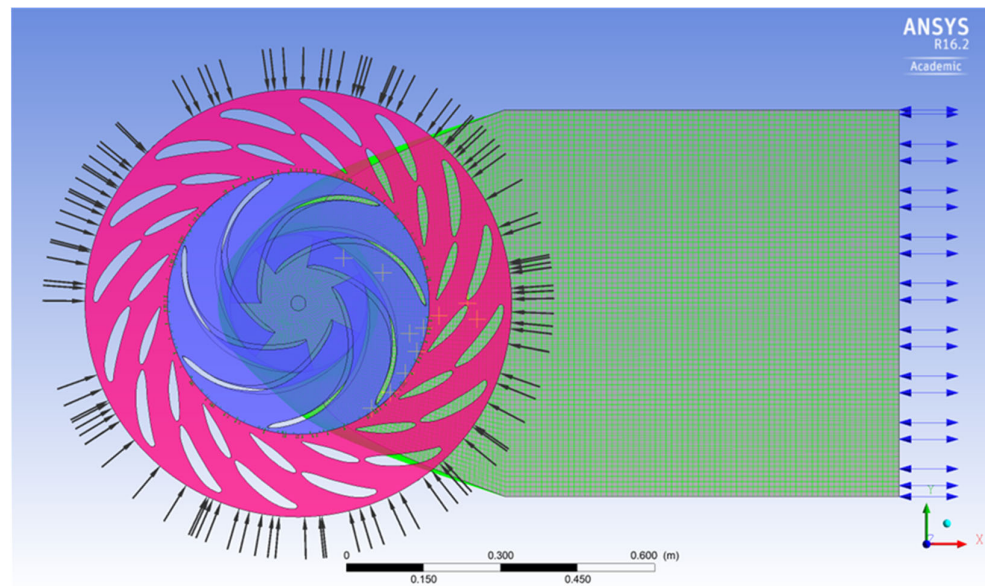


**Figure 2.** Top view of the computational domain for the case study.

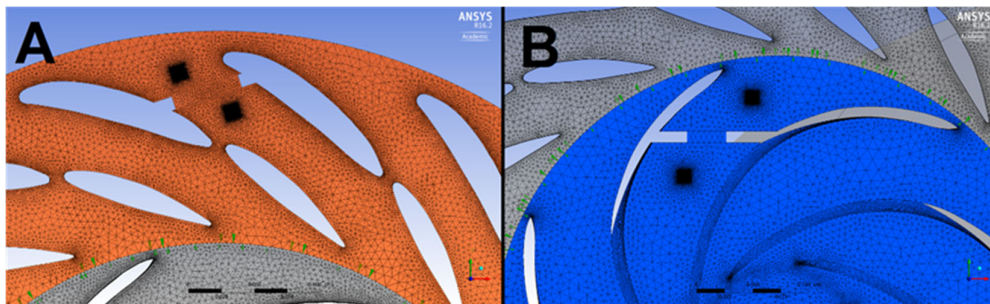


**Figure 3.** Detail of the geometrical model and computational mesh for the studied cases: (A) distributor channel blockage and (B) rotor channel blockage.

### 2.3. Numerical Procedure

Unsteady-state numerical simulations for the machine's best efficiency point were carried out using Ansys® CFX v16.2 CFD software, Canonsburg, PA, USA, which simultaneously solves continuity and Navier–Stokes equations for a fluid in motion.

The boundary conditions imposed consisted of the rotor rotational speed (3435 rpm), mass flow rate (953 kg/s) and flow direction (parallel to the guide vane chord) at the distributor inlet and a reference pressure at the draft tube outlet. The time step selected for the unsteady analysis corresponded to a  $1^\circ$  rotation of the runner [19]. An SST  $k-\omega$  turbulence model [20] was used to compute the turbulent flow quantities, for which a turbulence intensity of 5% was used as a boundary condition at the stator inlet.

Ansys® CFX uses the finite volume method for spatial discretization. A high-resolution advection scheme (which consists of a numerical advection scheme with a calculated blending factor) was selected for the stabilization of the convective term. Time discretization was achieved by a 2nd-order backward Euler scheme. Tri-linear finite element-based functions were used as an interpolation scheme. Ansys® CFX uses a coupled solver which solves the Navier–Stokes equations (for velocity components and pressure) as a single system. First, non-linear equations are linearized (coefficient iteration), and then these linear equations are solved by an algebraic multigrid (AMG) solver. For convergence criteria, residual types were set to the root mean square (RMS) value of the normalized residuals with a target value of  $1 \times 10^{-3}$ . Simulations were carried out on a 64-bit, Intel core i7

processor (6 core|12 thread) @ 3.3 GHz and 32 GB RAM, with simulation times of about 60 to 110 h (depending on the studied case) to reach quasi-steady flow conditions in all regions of the model.

To characterize the effect of ingested bodies on the RSI of the modeled pump turbine, pressure fluctuations in time were recorded for all studied cases. To capture the unsteady pressure pulse, pressure monitoring points were added to the rotor (R1, R2, R3), distributor (E1, E2, E3) and radial gap (IF3, IF4, IF5) of the machine (Figure 4). For obstructed flow cases, pressure monitoring regions were added upstream and downstream of the obstruction (Figure 3).

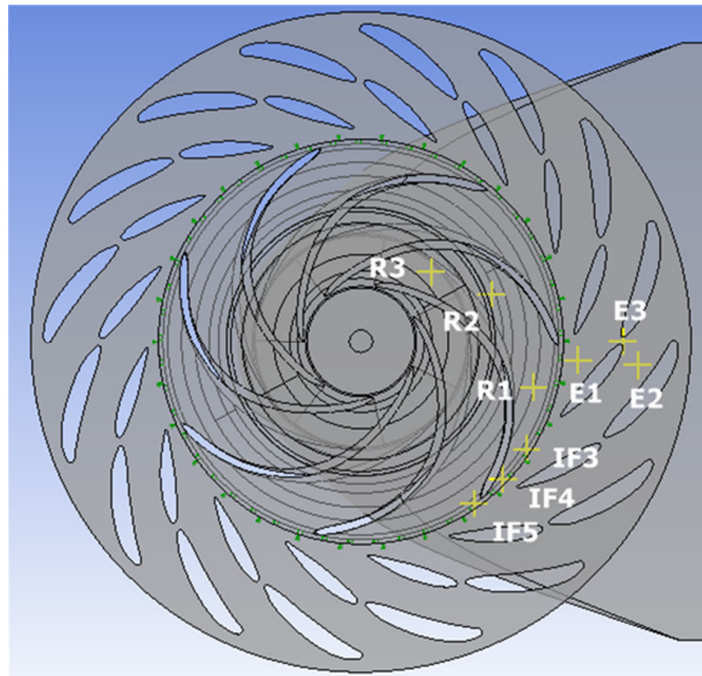


**Figure 4.** Location of the pressure monitoring points used.

#### 2.4. Post-Processing and Data Analysis

For all studied cases, the recorded temporal pressure signals were processed using a fast Fourier transform (FFT) algorithm [21,22]. These signals consisted of 0.5 s of flow time, recorded once the computational model reached quasi-steady state (i.e., when the oscillating pressure signal period and amplitude stabilized). This quasi-steady state was reached after 20 to 30 runner revolutions, depending on the studied case. Sampling frequency was set to 20,610 Hz for all cases, resulting in a 2 Hz frequency resolution for the frequency spectra obtained. These spectra were analyzed in order to complement the information extracted from the recorded pressure data.

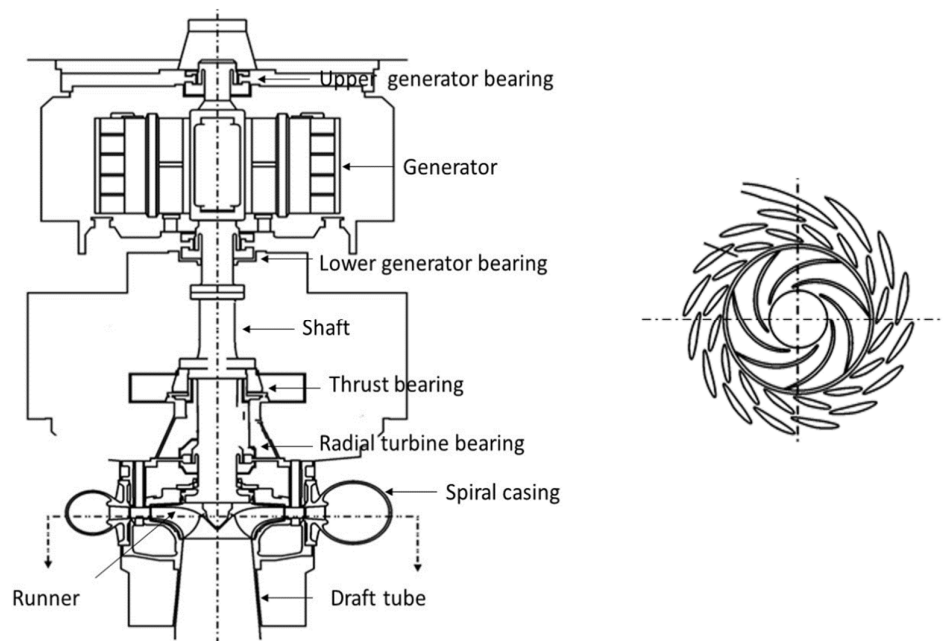
### 3. Results and Discussion

#### 3.1. Validation of the Numerical Simulations

CFD as a modeling tool has been extensively validated in hydraulic turbine applications [23]. In order to validate the CFD simulations performed in this study, the numerical results obtained for the pressure pulse in an unobstructed pump turbine CFD model were compared against experimental data obtained on a pump turbine prototype geometrically similar to the aforementioned computational model.

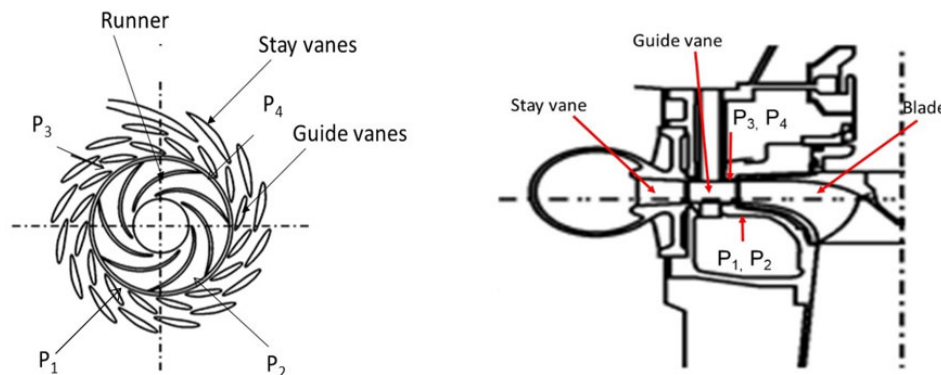
A schematic representation of the pump turbine prototype is shown in Figure 5. The pump turbine prototype is designed for a net head of 376 m and a volumetric flow rate of

32 m<sup>3</sup>/s. The rotating speed of the pump turbine unit is 600 rpm, the runner has a diameter of 2.87 m and its nominal power is about 100 MW.



**Figure 5.** Schematic representation of the pump turbine prototype from the experimental study.

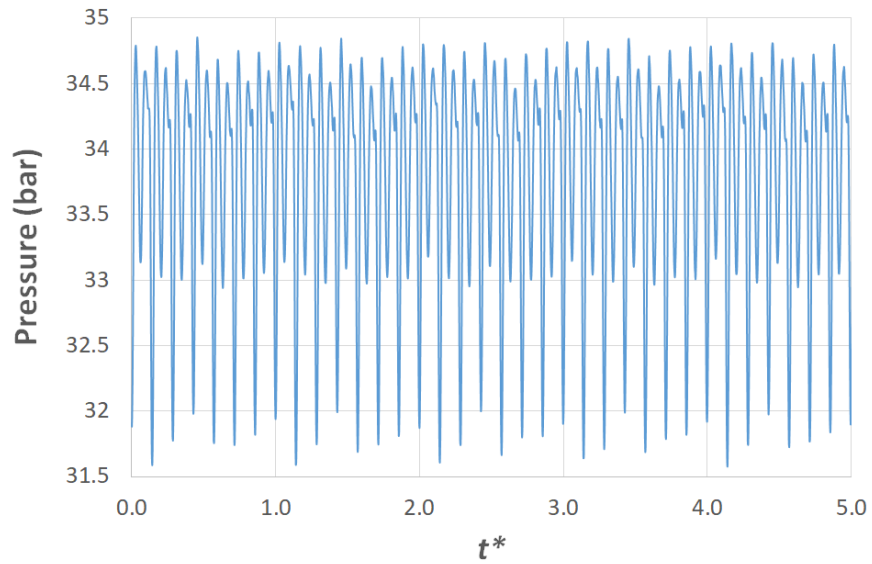
Experimental measurements on the pump turbine prototype were carried out by members of this research group. For these experimental tests, four pressure transducers were installed at different locations of the prototype's head cover. These locations are shown in Figure 6. Additional details on the experiments and the obtained results can be found in [24].



**Figure 6.** Location of the pressure transducers installed for the experimental study [24].

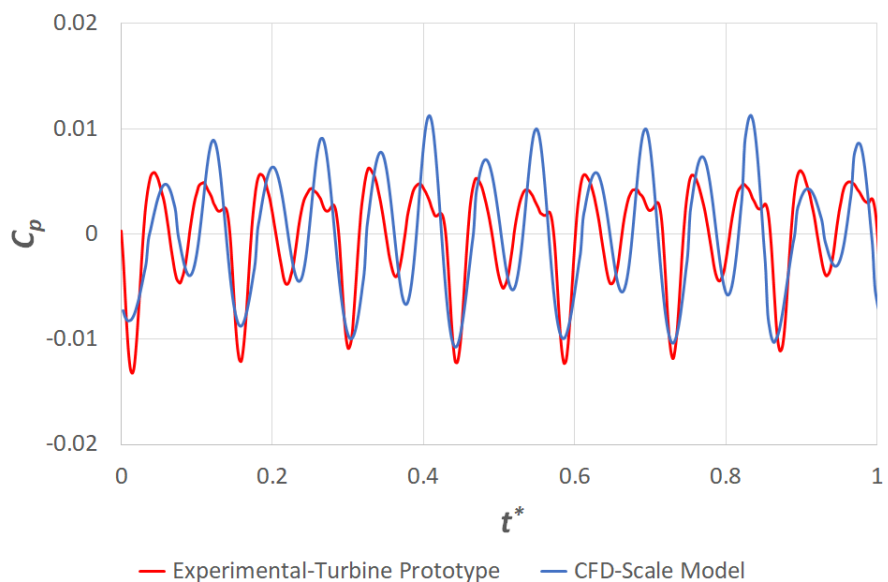
Wika S-10 pressure transducers were used for the experimental measurements [25]. The transducers' sensitivity is 0.2 mV/bar ( $\pm 5\%$ ), and their frequency range is 0–1000 Hz ( $\pm 10\%$ ). The pressure signals registered by these transducers were conditioned using a 16-channel conditioner, Bruel & Kjaer model 2694 [26], and recorded with a Sony PC216Ax data recorder with 16 bits of resolution and a frequency range of 0–20,000 Hz ( $\pm 10\%$ ) [27]. Figure 7 shows an example of the pressure fluctuation due to rotor–stator interaction

measured by the transducers, plotted vs. normalized time  $t^*$  (using the time of one revolution of the runner as a reference value).



**Figure 7.** Pressure signal recorded at location P1 for BEP turbine prototype operation.

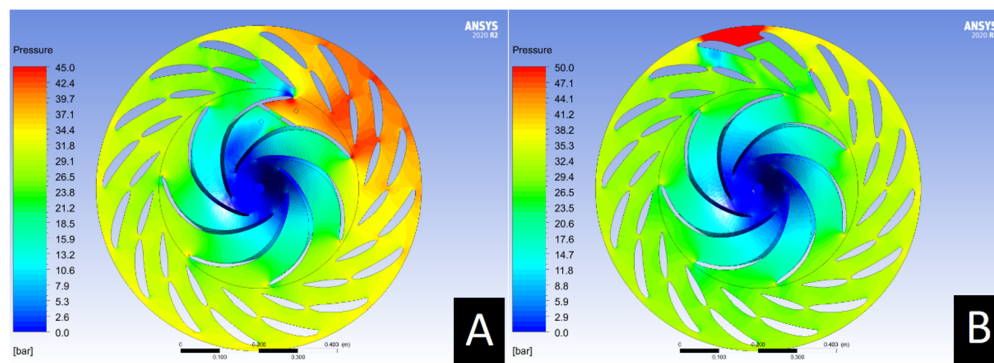
The dimensionless pressure signals obtained at the distributor for both the prototype and the CFD pump turbine model, reported as the machine's coefficient of pressure ( $C_p$ ), are shown in Figure 8. As it can be seen, the CFD model is able to reproduce the oscillating nature of the pressure pulse in the machine distributor. The computational results capture both the frequency and the amplitude of the pressure pulse with enough accuracy when compared against the experimental data, validating our numerical model. The differences observed between the experimental and the CFD dimensionless pressure signals can be attributed to the geometric simplifications used in the CFD model, which did not include the machine's inlet volute or the breakwater.



**Figure 8.** Coefficient of pressure ( $C_p$ ) vs. normalized time ( $t^*$ ) for pump turbine model (CFD) and prototype (experimental).

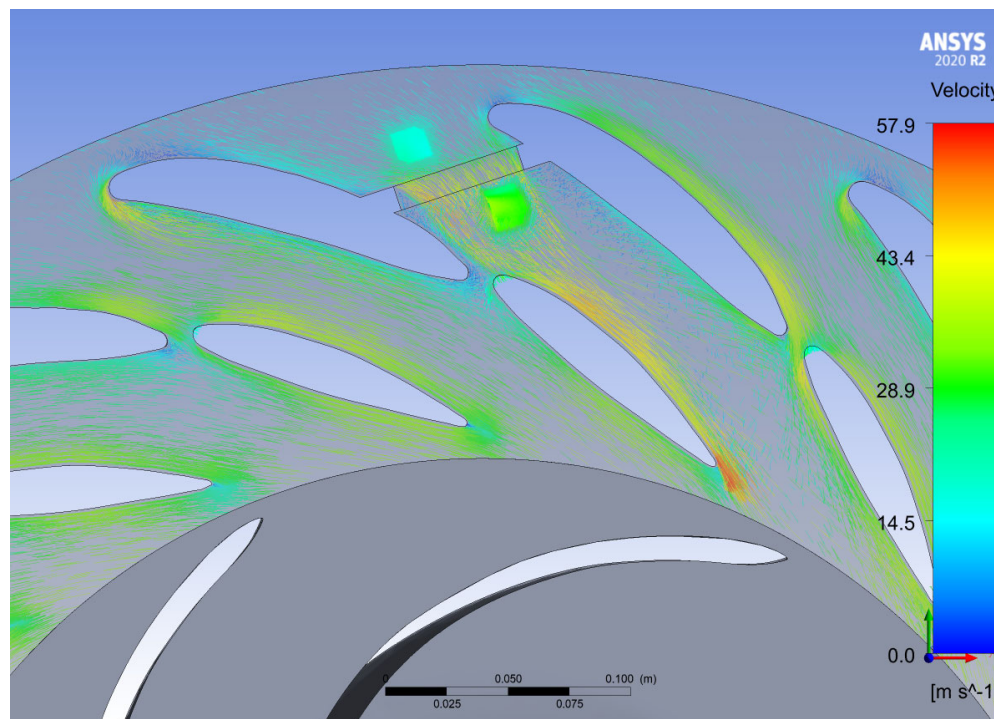
### 3.2. Pressure/Velocity Plots for Blockage Cases

Figure 9 shows an example of the pressure contours obtained for the rotor and distributor blockage cases. For all studied cases, a channel blockage creates a high-pressure region in the machine's distributor. In the case of a rotor blockage, this high-pressure region travels through the distributor at a rotation speed equal to the runner speed, while in the case of a distributor blockage, the high-pressure region remains confined to the blocked channel.



**Figure 9.** Example of pressure contours obtained for studied cases: (A) obstructed rotor; (B) obstructed distributor.

It could also be observed that for all blockage cases studied, low-pressure regions formed downstream the blocked channel, reaching pressure values that could potentially initiate cavitation near the downstream rotor blade's leading edge, in the case of a rotor blockage (Figure 9A). These low-pressure regions are a result of the acceleration experienced by the flow deviated by the blockage as it is throttled by the downstream distributor vane/rotor blade into the following channel (Figures 10 and 11).



**Figure 10.** Velocity vector plot near the blockage for a 50% obstructed distributor.

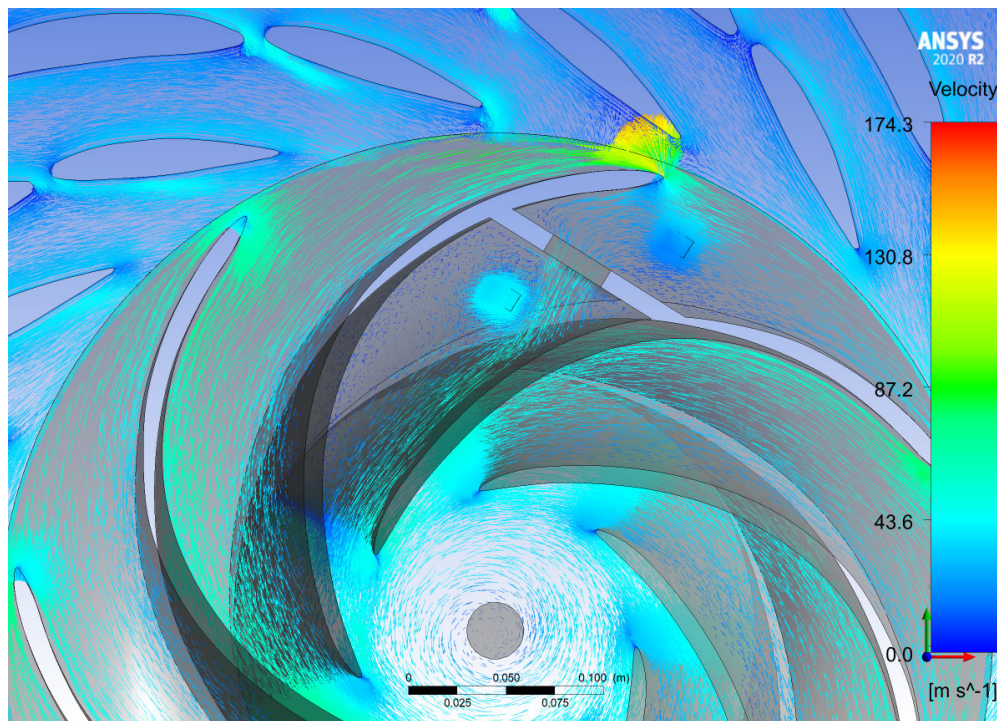


**Figure 11.** Relative velocity vector plot near the blockage for a 25% obstructed rotor.

### 3.3. Obstructed Rotor Analysis

#### 3.3.1. Effect of the Blockage Size

CFD models were created for three rotor blockage scenarios: 25, 50 and 75% of the rotor channel cross-section area blocked at  $0.5D$ . In order to characterize the effect of the blockage size on the machine RSI, the results obtained were compared against those obtained for an unobstructed pump turbine. Figures 12 and 13 show the pressure signals obtained for different blockage sizes in a rotor channel, both for the inertial (distributor) and the moving (rotor) reference frame, respectively.

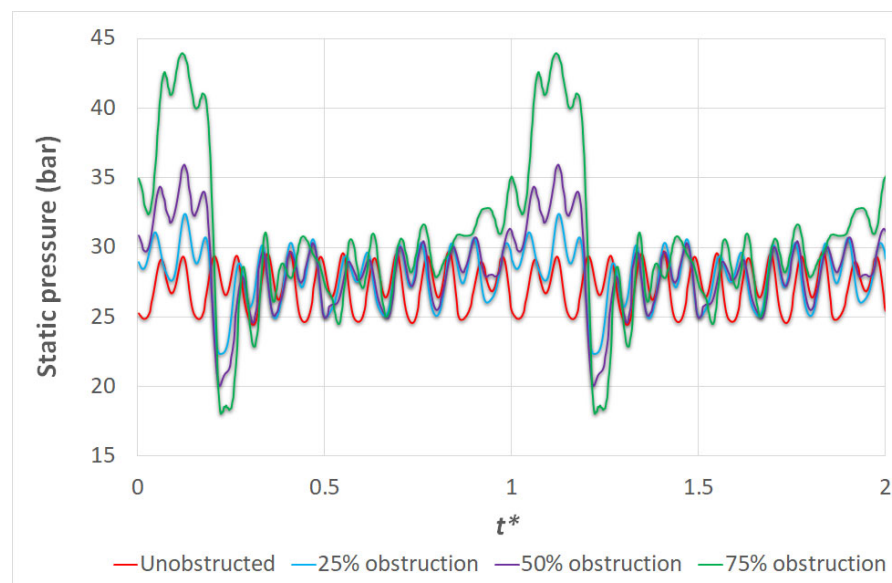


**Figure 12.** Pressure signal in the inertial reference frame (monitor point E3) for different rotor blockage sizes.

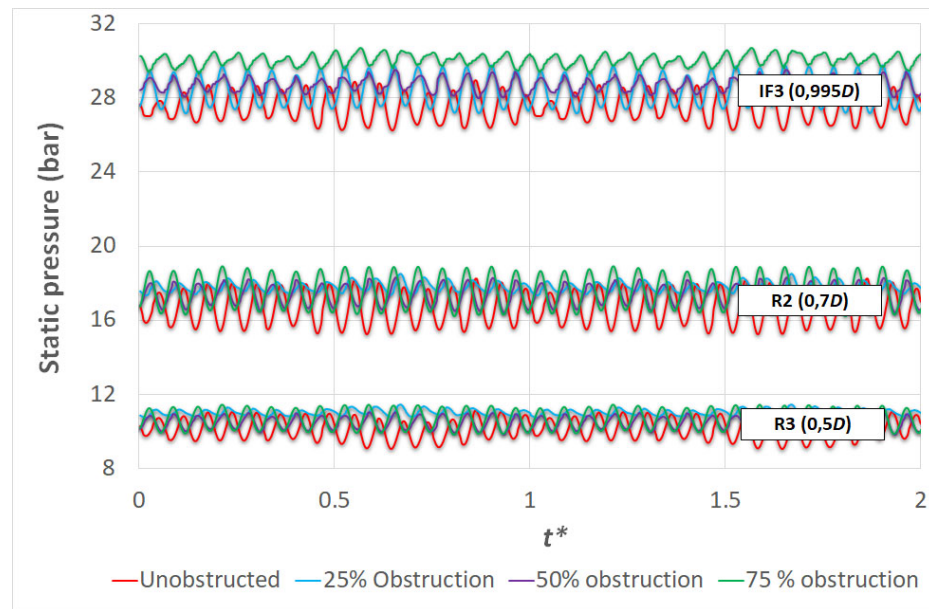


**Figure 13.** Pressure signal in the rotating reference frame for different rotor blockage sizes.

It can be observed in Figure 12 that once per rotation cycle, the rotor blockage amplifies the pressure pulse in the inertial reference frame. The amplitude of this pressure pulse increases with the blockage size. In the rotating reference frame (Figure 13), the most noticeable fact is that pressure values in the rotor for all obstructed cases studied are higher than those recorded for the unobstructed rotor case. It can also be noticed that a runner blockage causes a damping on its pressure fluctuation.

Figures 14 and 15 show an example of the frequency spectra obtained from the pressure signals registered in the inertial and rotating reference frames, respectively. In the inertial reference frame (Figure 14), the pressure pulse characteristic frequency for the unobstructed rotor case is  $2 \cdot f_b = 801.50$  Hz, typical of pump turbines [28]. An obstructed rotor channel excites the runner rotation frequency  $f_f = 57.25$  Hz and its harmonics. This is consistent with the behavior reported by Egusquiza et al. (2010) [15]. The runner blockage produces axial and radial hydraulic force imbalances that rotate at the runner frequency, causing increased vibration levels in the machine. It can also be observed that the amplitude of this vibration increases with the blockage size, due to larger force imbalances generated by larger obstructions.

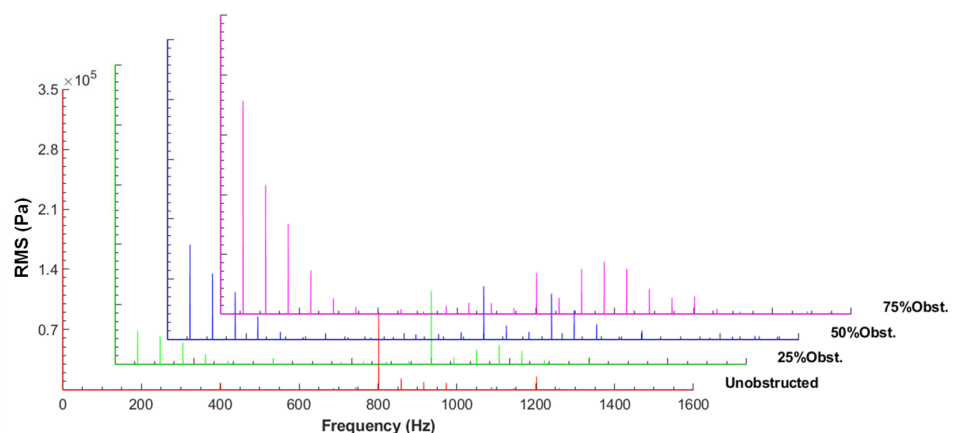


**Figure 14.** Frequency spectra in the inertial reference frame (monitor point E2) for different rotor blockage sizes.

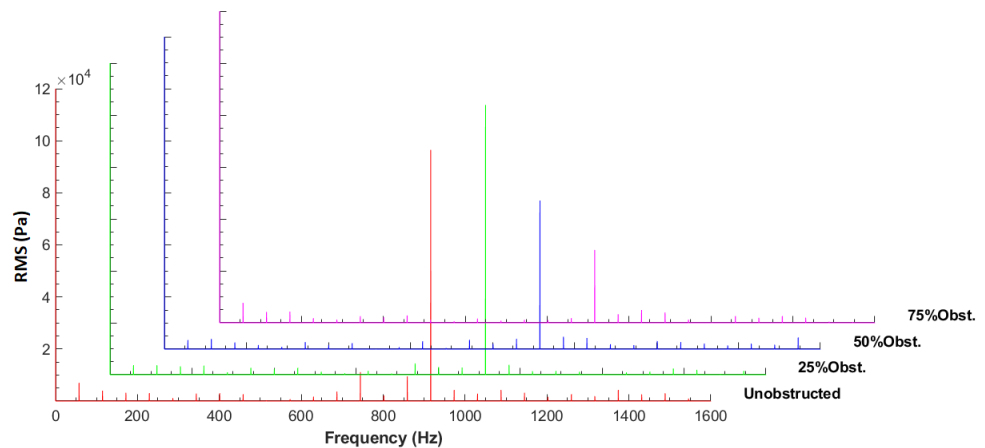


**Figure 15.** Frequency spectra in the rotating reference frame (monitor point R1) for different rotor blockage sizes.

In the rotating reference frame (Figure 15), the pressure pulse characteristic frequency for the unobstructed rotor case is  $f_p = 916$  Hz. In this case, a rotor channel obstruction does not excite any other characteristic frequencies. It can also be clearly observed that the damping on the runner pressure signal observed in Figure 11 is relevant for large runner obstructions. Signal amplitude decreases are observed for 50 and 75% runner obstructions, with the signal damping increasing with the blockage size, but the 25% obstruction case presents amplitude levels similar to the unobstructed case.

### 3.3.2. Effect of Blockage Position

CFD models were created for three rotor blockage scenarios: 50% of the rotor channel cross-section area blocked at  $0.4D$ ,  $0.6D$  and  $0.8D$ . To characterize the effect of the rotor blockage position on the machine RSI, the results obtained were compared against those obtained for an unobstructed pump turbine. Figures 16 and 17 show an example of the frequency spectra obtained from the pressure signals registered in the inertial and rotating reference frames, respectively.

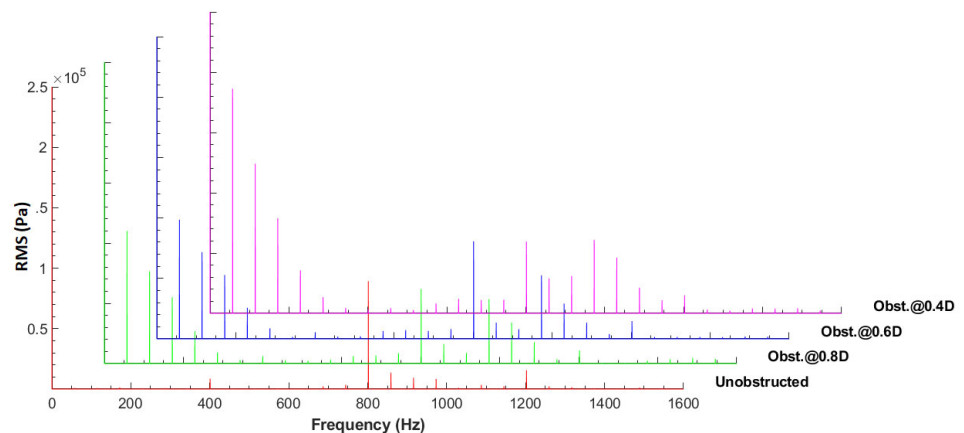


**Figure 16.** Frequency spectra in the inertial reference frame (monitor point E2) for different rotor blockage positions.

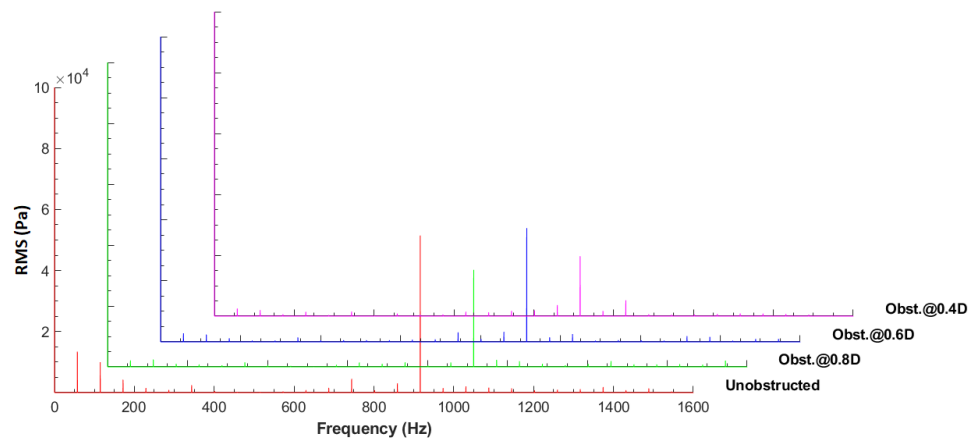


**Figure 17.** Frequency spectra in the rotating reference frame (monitor point R3) for different rotor blockage positions.

It can be observed that for the inertial reference frame (Figure 16), the excitation amplitude of the runner rotation frequency is larger when the blockage is located closer to the turbine axis. In this region, flow velocities are high due to the reduction in the cross-section area. A further reduction in the flow area due to an ingested body would generate even larger velocities, thus creating a larger hydraulic force unbalance. Therefore, a small object stuck closer to the runner blade trailing edge would cause a larger increase in the machine's vibration levels than a larger object stuck closer to its leading edge. In the rotating reference frame (Figure 17), pressure signal damping similar to that observed in Figure 13 occurs, where larger hydraulic force unbalances lead to larger damping of the pressure oscillation in the runner.

### 3.4. Obstructed Distributor Analysis

CFD models were created for two distributor blockage scenarios, in which 50% and 100% of the distributor channel cross-section area are blocked, located between two guide vanes. To characterize the effect of the distributor blockage position on the machine RSI, the results obtained were compared against those obtained for an unobstructed pump turbine. Figures 18 and 19 show the pressure signals obtained for different blockage sizes in a rotor channel, both for the inertial (distributor) and the moving (rotor) reference frame, respectively.

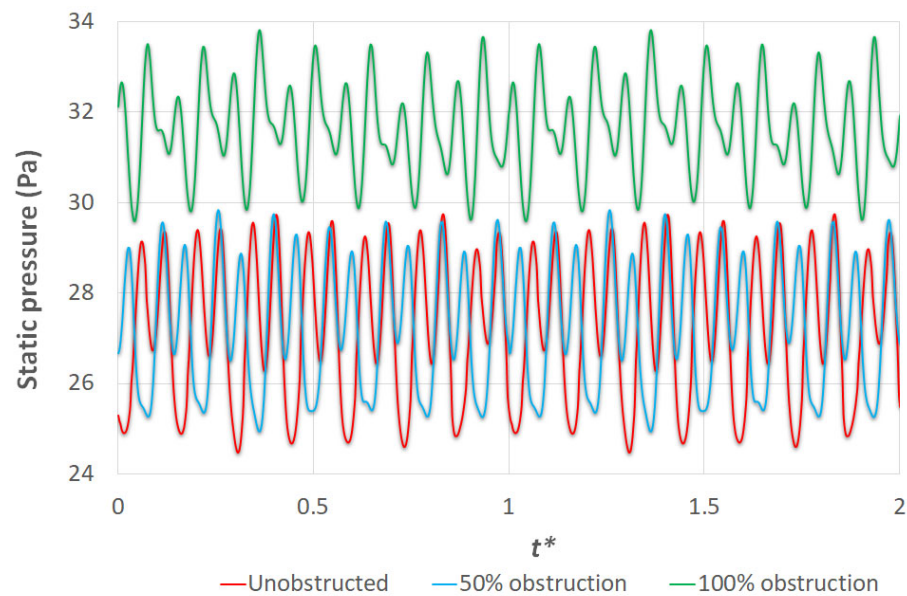


**Figure 18.** Pressure signal in the inertial reference frame (monitor point E3) for different distributor blockage sizes.

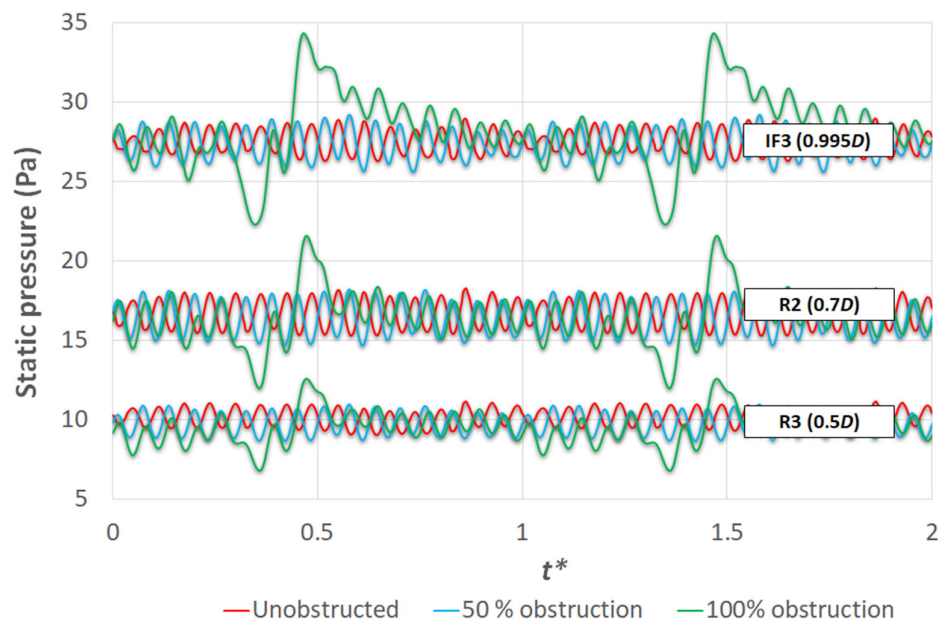


**Figure 19.** Pressure signal in the rotating reference frame for different distributor blockage sizes.

In the inertial reference frame (Figure 18), it can be noticed that a partial distributor blockage has little effect on the pressure pulse. Pressure values in the distributor increase with a total blockage in one of its channels. The blockage effects are also visible in the frequency domain (Figure 20), where a slight reduction in the pressure pulse amplitude can be observed for a total blockage of a distributor channel.

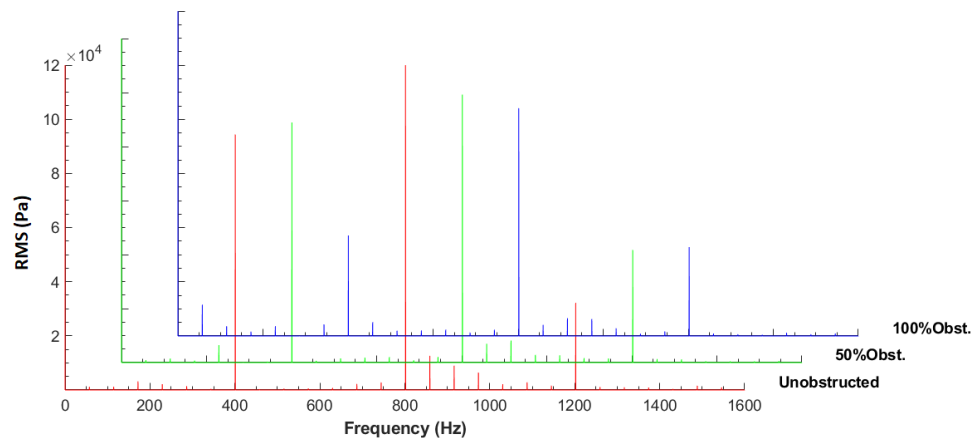


**Figure 20.** Frequency spectra in the inertial reference frame (monitor point E1) for different distributor blockage sizes.

In the rotating reference frame (Figure 19), a partial distributor blockage seems to have limited effects on the pressure pulse recorded at different rotor diameters. In the frequency domain (Figure 21), it can be noticed that this partial obstruction excites the higher harmonics of the runner rotation frequency, agreeing with the observations of the case study reported by Egusquiza et al. (2010) [15]. Larger obstruction sizes will tend to excite lower harmonics of the runner rotation frequency, and this excitation will have larger amplitudes. A distributor blockage creates a non-uniform flow and pressure distribution at the runner–distributor interface, and this disruption of the circumferential uniformity of the flow entering the runner will increase with the blockage size, affecting the runner’s radial force equilibrium.

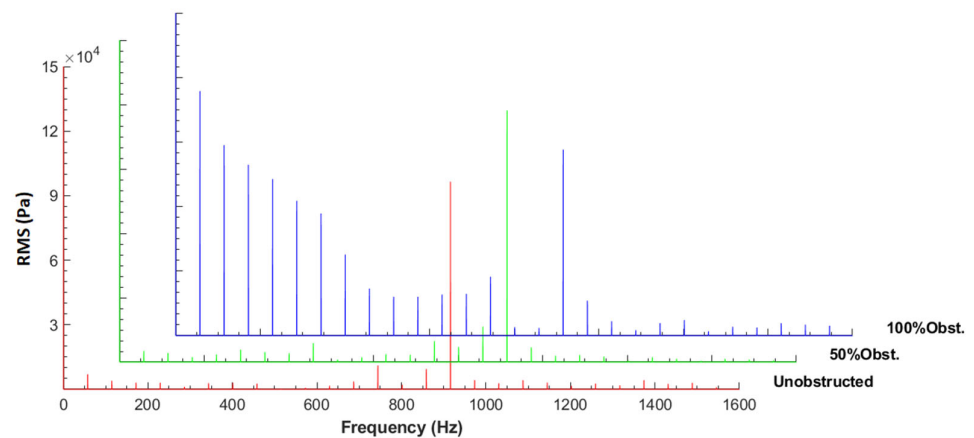


**Figure 21.** Frequency spectra in the rotating reference frame (monitor point R1) for different distributor blockage sizes.

#### 4. Conclusions

The work presented shows the potential offered by modern CFD for studying turbomachinery problems which otherwise would be difficult or expensive to investigate experimentally. In this study, a numerical model was used to assess the effect of the size and location of runner and distributor blockages on the RSI pressure pulse of a pump turbine. The numerical model was validated against experimental data measured on an unobstructed prototype, finding it suitable for the purposes of the study.

Runner obstructions generate unbalanced radial hydraulic forces that rotate at the runner frequency, causing increased vibration levels in the machine. The perturbation

caused by a runner obstruction on the machine pressure signal can be clearly detected in the inertial reference frame. The amplitude of the pressure fluctuations in the pump turbine distributor increases with the blockage size, due to larger force imbalances generated by larger obstructions.

In the runner, the perturbation caused by the blockage manifested as a damping of the pressure signal, but only on large blockages. Decreases in the pressure signal amplitude were observed for 50 and 75% runner obstructions, with the signal damping increasing with the blockage size, but the 25% obstruction case presented amplitude levels similar to the unobstructed runner case. It was also observed that the excitation amplitude of the runner rotation frequency was larger when the blockage was located closer to the turbine axis. An ingested body in such a geometry-constricted zone of the machine creates larger hydraulic force unbalances due to the flow acceleration around it.

Blockage in the distributor affects the pressure pulse in the runner. For partial blockages, this pressure disturbance excites higher-order harmonics of the runner rotation frequency. Larger distributor blockages manifest through the excitation of lower-order harmonics together with increased vibration amplitudes. This is mainly caused by the greater force unbalance generated by the flow and pressure non-homogeneity the obstruction creates at the rotor–stator interface.

**Author Contributions:** Conceptualization, E.E. and A.G.; methodology, A.G.; software, A.F.; validation, C.V., A.F. and A.G.; investigation, A.F. and A.G.; writing—original draft preparation, M.E.; writing—review and editing, A.G. All authors have read and agreed to the published version of the manuscript.

**Funding:** Funding from the European Union’s Horizon 2020 research and innovation programme (H2020-857832-XFLEX) is acknowledged.

**Conflicts of Interest:** The authors declare no conflict of interest.

### Nomenclature

$C_p$	Coefficient of pressure	$C_p = \Delta p / ((\rho(\omega D)^2)$
$D$	Runner diameter	m
$f_b$	Runner blade passing frequency	Hz
$f_f$	Runner rotation frequency	Hz
$f_v$	Distributor vane passing frequency	Hz
$g$	Standard gravity	9.81 m/s <sup>2</sup>
$H$	Pump turbine net head	m
$N$	Runner rotation speed	rpm
$N_s$	Dimensionless runner specific speed	$N_s = \omega V^{1/2} / (gH)^{3/4}$
$p$	Pressure	Pa
$t^*$	Dimensionless time	$t^* = t / t_{cycle}$
$t$	Time	s
$t_{cycle}$	Time of 1 runner revolution	s
$V$	Volumetric flow rate	m <sup>3</sup> /s
$y^+$	Dimensionless wall distance	-
$z_b$	Number of runner blades	-
$z_v$	Number of distributor vanes	-

### Greek letters

$\rho$	Density	kg/m <sup>3</sup>
$\omega$	Runner rotation speed	rad/s

### Acronyms

AMG	Algebraic multigrid
BEP	Best efficiency point
CFD	Computational fluid dynamics

FFT	Fast Fourier transform
RMS	Root mean square
RSI	Rotor–stator interaction

## References

- Gaudard, L.; Romerio, F. The future of hydropower in Europe: Interconnecting climate, markets and policies. *Environ. Sci. Policy* **2014**, *37*, 172–181, <https://doi.org/10.1016/j.envsci.2013.09.008>.
- Dorji, U.; Ghomashchi, R. Hydro turbine failure mechanism: An overview. *Eng. Fail. Anal.* **2014**, *44*, 136–147, <https://doi.org/10.1016/j.engfailanal.2014.04.013>.
- Frunzăverde, D.; Muntean, S.; Mărginean, G.; Câmpian, V.; Marşavina, L.; Terzi, R.; Şerban, V. Failure analysis of a Francis turbine runner. *IOP Conf. Ser. Earth Environ. Sci.* **2010**, *12*, 012115, <https://doi.org/10.1088/1755-1315/12/1/012115>.
- Egusquiza, E.; Valero, C.; Huang, X.; Jou, E.; Guardo, A.; Rodríguez, C. Failure investigation of a large pump-turbine runner. *Eng. Fail. Anal.* **2012**, *23*, 27–34, <https://doi.org/10.1016/j.engfailanal.2012.01.012>.
- Brekke, H. Performance and safety of hydraulic turbines. *IOP Conf. Ser. Earth Environ. Sci.* **2010**, *12*, 012061, <https://doi.org/10.1088/1755-1315/12/1/012061>.
- Liu, X.; Luo, Y.; Wang, Z. A review on fatigue damage mechanism in hydro turbines. *Renew. Sustain. Energy Rev.* **2016**, *54*, 1–14, <https://doi.org/10.1016/j.rser.2015.09.025>.
- Liu, X.; Luo, Y.; Presas, A.; Wang, Z.; Zhou, L. Cavitation effects on the structural resonance of hydraulic turbines: Failure analysis in a real Francis turbine runner. *Energies* **2018**, *11*, 2320, <https://doi.org/10.3390/en11092320>.
- Thapa, B.S.; Dahlhaug, O.G.; Thapa, B. Sediment erosion in hydro turbines and its effect on the flow around guide vanes of Francis turbine. *Renew. Sustain. Energy Rev.* **2015**, *49*, 1100–1113, <https://doi.org/10.1016/j.rser.2015.04.178>.
- Kjølle, A. Hydropower in Norway. Mechanical Equipment. Trondheim: Norwegian University of Science and Technology. 2001. Available online: <https://www.ntnu.no/documents/381182060/641036380/Mechanical+Equipment+Kjolle+ny.pdf/> (accessed on 1 October 2021).
- Simoneau, R. The optimum protection of hydraulic turbines against cavitation erosion. In Proceedings of the 12th IAHR Symposium, Stirling, UK, 27–30 August 1984.
- Padhy, M.K.; Saini, R.P. A review on silt erosion in hydro turbines. *Renew. Sustain. Energy Rev.* **2007**, *12*, 1975–1986, <https://doi.org/10.1016/j.rser.2007.01.025>.
- Neopane, H.P. Sediment Erosion in Hydro Turbines. Ph.D. Thesis, Norwegian University of Science and Technology, Trondheim, Norway, 2010.
- Neopane, H.P.; Sujakhu, S.; Shrestha, S.; Subedi, K.; Basnet, A. Study of sediment erosion in hydraulic turbine using rotating disc apparatus. In Proceedings of the 2nd International Conference on the Developments in Renewable Energy Technology (ICDRET 2012), Dhaka, Bangladesh, 5–7 January 2012; pp. 1–4.
- Huang, X.; Valero, C.; Egusquiza, E.; Presas, A.; Guardo, A. Numerical and experimental análisis of the Dynamic response of large submerged trash-racks. *Comput. Fluids* **2013**, *71*, 54–64, <https://doi.org/10.1016/j.compfluid.2012.09.016>.
- Egusquiza, E.; Valero, C.; Estévez, A.; Guardo, A.; Coussirat, M. Failures due to ingested bodies in hydraulic turbines. *Eng. Fail. Anal.* **2011**, *18*, 464–473, <https://doi.org/10.1016/j.engfailanal.2010.09.039>.
- Rodríguez, C.G.; Egusquiza, E.; Santos, I.F. Frequencies in the vibration induced by the rotor stator interaction in a centrifugal pump turbine. *J. Fluids Eng.* **2007**, *129*, 1428–1435, <https://doi.org/10.1115/1.2786489>.
- Mathur, S.R. Unsteady flow simulations using unstructured sliding meshes. In Proceedings of the Fluid Dynamics Conference, Colorado Springs, CO, USA, 20–23 June 1994; American Institute of Aeronautics and Astronautics: Reston, VA, USA, 1994, <https://doi.org/10.2514/6.1994-233>.
- Nicolle, J.; Giroux, A.M.; Morissette, J.F. CFD configurations for hydraulic turbine startup. *IOP Conf. Ser. Earth Environ. Sci.* **2014**, *22*, 032021, <https://doi.org/10.1088/1755-1315/22/3/032021>.
- Simpson, A.T.; Spence, S.W.T.; Watterson, J.K. A comparison of the flow structures and losses within vaned and vaneless stators for radial turbines. *J. Turbomach.* **2009**, *131*, 031010, <https://doi.org/10.1115/1.2988493>.
- Menter, F.R. Two-equation eddy-viscosity turbulence models for engineering applications. *AIAA J.* **1994**, *32*, 1598–1605, <https://doi.org/10.2514/3.12149>.
- Cooley, J.W.; Lewis, P.A.W.; Welch, P.D. Historical notes on the fast Fourier transform. *IEEE Trans. Audio Electroacoust.* **1967**, *15*, 76–79, <https://doi.org/10.1109/TAU.1967.1161903>.
- Welch, P.D. The use of fast Fourier transform for the estimation of power spectra: A method based on time averaging over short, modified periodograms. *IEEE Trans. Audio Electroacoust.* **1967**, *15*, 70–73, <https://doi.org/10.1109/TAU.1967.1161901>.
- Trivedi, C.; Cervantes, M.J.; Dahlhaug, O.G. Numerical techniques applied to hydraulic turbines: A perspective review. *Appl. Mech. Rev.* **2016**, *68*, 010802, <https://doi.org/10.1115/1.4032681>.
- Rodríguez, C.G.; Mateos-Prieto, B.; Egusquiza, E. Monitoring of rotor-stator interaction in pump-turbine using vibrations measured with on-board sensors rotating with shaft. *Shock Vib.* **2014**, *2014*, 276796, <https://doi.org/10.1155/2014/276796>.
- WIKA Alexander Wiegand SE & Co. KG, High-Quality Pressure Transmitters—Model S-10. Available online: [https://en.wika.com/s\\_10\\_en\\_co.WIKA](https://en.wika.com/s_10_en_co.WIKA) (accessed on 7 August 2021).

26. Brüel & Kjær A/S, 16-Channel CCLD Signal Conditioner | Type 2694-A |. Available online: <https://www.bksv.com/en/transducers/signal-conditioning/cclcd/2694-a> (accessed on 7 August 2021).
27. Sony Presicion Technology Inc., Portable DAT Instrumentation Recorder PC200Ax Series. Available online: <https://www.daqlong-systems.co.uk/support/obsolete-systems/item/16-pc200-series> (accessed on 7 August 2021).
28. Egusquiza, E.; Valero, C.; Valentín, D.; Presas, A.; Rodríguez, C.G. Condition monitoring of pump-turbines. New challenges. *Measurement* **2015**, *67*, 151–163, <https://doi.org/10.1016/j.measurement.2015.01.004>.